Photoluminescence transitions in semiconductor superlattices. Theoretical calculations for InGaN blue laser device

A. Kunold[a] and P. Pereyra
Area de Física Teórica y Materia Condensada, Universidad Autónoma Metropolitana-A, Av. S. Pablo 180, Col. Reynosa-Tamaulipas, México D.F. 02200, México

(Received 16 September 2002; accepted 12 February 2003)

The optical response of an AlGaN/GaN/$(In_xGa_{1-x}N)^n$/GaN/AlGaN heterostructure is obtained from precise, and comparatively simple, transition probability calculations. A comprehensive approach to evaluate these quantities from rigorous expressions of the heterostructure's energy eigenvalues and eigenfunctions is given. Taking full account of the longitudinal quantum wells and the lateral quantum dot confinement, quite precise intraband energy levels and wave functions have been obtained. Photoluminescence results for sectionally constant band-edge profile differ from the experimental measurements by approximately 45 meV. We show that the band-edge modulation arising from charge polarization, is responsible for this difference. © *2003 American Institute of Physics.* [DOI: 10.1063/1.1565698]

I. INTRODUCTION

In recent years, the increasing interest in short wavelength emitting diodes and blue laser devices has led to overwhelming experimental and theoretical activity.[1–8] Extensive attention has been devoted to heterostructures growing procedures and to the understanding of the principal elements that contribute to the optical response of these systems. To obtain lower current-density threshold, the proper wavelength, and reduced temperature sensitivity, distinct multilayer AlInGaN heterostructures have been produced. The most successful structures for laser devices contain an active region of $(In_{x_1}Ga_{1-x_1}N/In_{x_2}Ga_{1-x_2}N)^n$ superlattice between the *p*- and *n*-doped $Al_{0.08}Ga_{0.92}N$ and GaN cladding layers (Fig. 1). Major advantages of these types of structures are a stronger confinement of electrons and holes and the formation of narrow and well separated subbands to provide higher monochromaticity, efficiency, and thermal stability.

Various characteristic properties of the AlInGaN heterostructures have been mentioned as relevant factors in the photon emission mechanism and their high performance. The formation of a large number of quantum dots because of width fluctuations in the layered structure and the high density of dislocations allow additional confinement and a larger number of *e-h* pairs. In Sec. II of this article, we introduce the theoretical basis to study the optical response taking into account both the longitudinal quantum wells and the lateral quantum dot confinement. We use the simple and closed formulas of the Theory of Finite Periodic Systems (TFPS), and the well-known formalism to evaluate the exciton's spectra.[9,10] A complete analysis of the transition probabilities is made assuming sectionally constant band-edge modulation. In this case, we were able to determine the superlattice energy eigenvalues $E^{c,v}_{\mu,\nu}$ (in the ν-th level and μ-th miniband of the conduction or valence bands), and the corresponding eigenfunctions $\Psi^{c,v}_{\mu,\nu}$. Based on this fundamental intraminiband information, we calculate the blue interband radiative recombination probabilities. We found out that the longitudinal confinement is responsible for the narrow and well-separated low-energy subbands. On the other hand, the attractive Coulomb interaction and the lateral quantum dot confinement increase the recombination probabilities. These features are necessary for a monochromatic emission, thermal stability, and an appropriate number of levels to enhance the population inversion mechanism.

In Sec. III, we apply the model for the specific $(In_{x_1}Ga_{1-x_1}N/In_{x_2}Ga_{1-x_2}N)^n$ heterostructure, and determine the optical response assuming sectionally constant band-edge profile. We obtain a two peak structure (Fig. 2). The major contribution for the lowest-energy peak at 2.92 eV comes from the radiative transition $E^c_{1,\nu}\rightarrow E^v_{1,\mu}$, and the peak at 3.155 eV from $E^c_{2,\nu}\rightarrow E^v_{2,\mu}$. The distance between these peaks differ from the photoluminescence (PL) measurements by approximately 45 meV. To explain this difference we introduce a brief and preliminary analysis of the charge polarization effect on the optical response. In recent years, the piezoelectric response and the spontaneous dielectric polarization, with localized two-dimensional electron and hole gases on opposite interfaces, have been observed for this type of system. This so-called ''quantum confining Stark effect'' modifies the potential profile and the minibands are displaced upward or downward. To obtain an insight of the charge polarization's role in the optical response, we use the potential obtained by Goepfert *et al.*[11] For this band-edge modulation we recalculate the energy eigenvalues and determine their shifts with respect to the sectionally constant potential case. Introducing these shifts we obtain a very good agreement with the experimental results (Fig. 2).

In Sec. IV we present our conclusions and discuss the possible extensions of the present model.

II. MODEL

We consider an exciton in a flat quantum dot located somewhere inside the heterostructure AlGaN/GaN/

[a]Electronic mail: akb@correo.azc.uam.mx

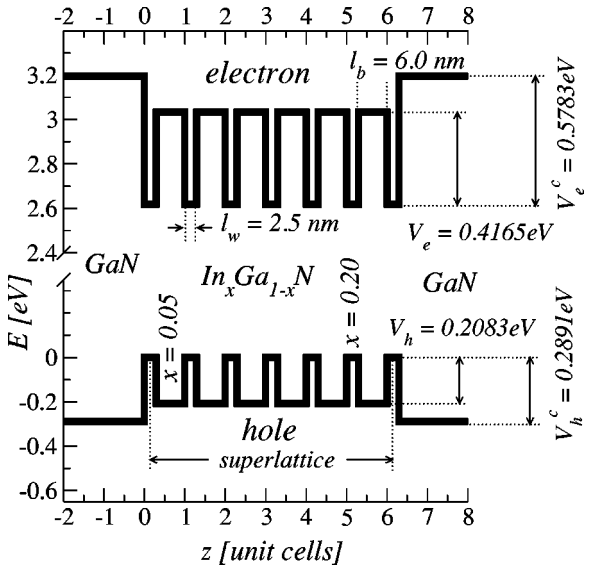

FIG. 1. Parameters of an AlGaN/GaN/$(In_{x_1}Ga_{1-x_1}N/In_{x_2}Ga_{1-x_2}N)^n$ /GaN/AlGaN heterostructure as reported by Nakamura *et al.*

$(In_{x_1}Ga_{1-x_1}N/In_{x_2}Ga_{1-x_2}N)^n$/GaN/AlGaN. In the growing direction the *e-h* pair is confined within the *n*-cell superlattice and the GaN buffer layers. This implies, in a first approximation, a finite periodic square-well modulation of the valence and conduction band edges along the growing *z* direction. In the *x-y* plane the confinement is modeled as a parabolic non symmetrical potential.[9] We are mainly interested here in the calculation of the optical susceptibility of this system. The expressions reported can be applied to different multilayer configurations. Besides the miniband structure, which determines the main contribution to the photoluminescence spectrum, we consider the quantum dot contribution to the confining excitonic energy. For this purpose we work in the effective mass approximation and solve, as explained below, the Schrödinger equation. The Hamiltonian operator is given by

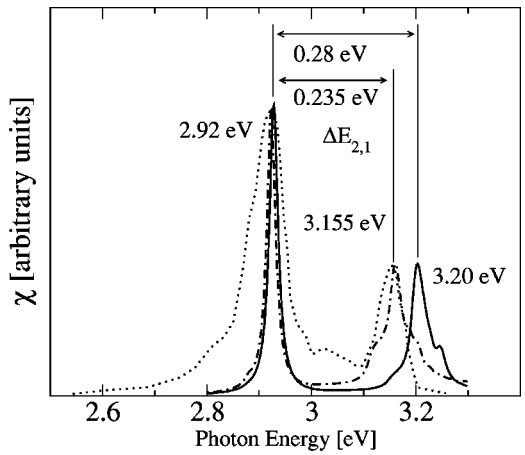

FIG. 2. Optical susceptibility and PL measurements as functions of the photon energy. The solid line (-) corresponds to our calculations of the optical susceptibility fitted to the PL measurements by Narukawa *et al.* (dotted line ...). The dashed line (-·-·-) shows the optical susceptibility taking into account the energy shift induced by charge polarization.

$$H=\sum_{q=e,h}(H_{\|q}+H_{\perp q}+H_{Iq})+H_{e-h}, \tag{1}$$

where *e* and *h* stand for electrons and holes, respectively. The operators $H_{\perp q}$, given by

$$H_{\perp q}=\frac{1}{2m^*_{\|q}}p^2_{zq}+V(z) \tag{2}$$

refer to the kinetic energy in the growing direction with effective mass $m^*_{\|q}$ and $V(z)$ the potential resulting from the band-edge modulation of the layered structure. This modulation is taken as a square-barrier superlattice bounded by GaN cladding layers. For the rest of this article, the inner part of the heterostructure will be referred to as the superlattice (Fig. 1).

For the *e-h* pair (confined by a transverse parabolic potential) we consider the Hamiltonian

$$H_{\perp q}=\frac{1}{2m^*_{\perp q}}(p^2_{xq}+p^2_{yq})+\frac{m^*_{\perp q}}{2}(\omega^2_x x^2_q+\omega^2_y y^2_q), \tag{3}$$

in which $m^*_{\perp q}$ is the transverse effective mass.

The particle-field interaction, to first order in the vector potential **A**, is given by

$$H_{Iq}=\pm\frac{e}{m^*_{\|q}c}\mathbf{A}\cdot\mathbf{p}. \tag{4}$$

The vector potential **A** of the photonic field is taken to be perpendicular to the propagation vector $\mathbf{K_s}$ of the electromagnetic field, which we expand into plane waves in the form

$$\mathbf{A}=\sqrt{\frac{2\pi\hbar c^2}{\Omega}}\sum_{s,\lambda}\sqrt{\frac{1}{\omega_s}}\mathbf{e_{s,\lambda}}(e^{i\mathbf{K_s}\cdot\mathbf{r}}d^+_{s,\lambda}+e^{-i\mathbf{K_s}\cdot\mathbf{r}}d_{s,\lambda}), \tag{5}$$

where Ω is a normalization volume. The orthogonal unitary polarization vectors $\mathbf{e}_{s,1}$ and $\mathbf{e}_{s,2}$ are at right angles to the propagation vector $\mathbf{K}_s$, and $d^+_{s,\lambda}$ and $d_{s,\lambda}$ are the photon creation and annihilation operators. The summation index *s* characterizes the direction and circular frequency ω_s of all possible wave components. Finally, $H_{e\text{-}h}$ describes the *e-h* Coulomb interaction

$$H_{e-h}=-\frac{e^2}{\epsilon\sqrt{(x_e-x_h)^2+(y_e-y_h)^2+(z_e-z_h)^2}}, \tag{6}$$

where ϵ is the permittivity of $In_xGa_{1-x}N$.

To decouple the *z*-axis motion from the *xy*-plane motion we rewrite the Coulomb interaction as

$$H_{e-h}=-\frac{e^2}{\epsilon\sqrt{(x_e-x_h)^2+(y_e-y_h)^2}}+\delta H_{e-h} \tag{7}$$

and treat $\delta H_{e\text{-}h}$ as a small perturbation that can be neglected.[9]

In the following subsections, we present new and old results of the TFPS applied to the specific device studied here.[10,12] We reformulate some expressions to determine the miniband structure, the energy eigenvalues, and eigenfunctions. We derive the transition and recombination probabili-

ties in the transfer matrix language of the TFPS to describe the particle-field interaction and the ensuing high-energy radiative recombination emissions.

A. Miniband structure, energy eigenvalues, and eigenfunctions

To obtain the energy eigenvalues and the corresponding eigenfunctions we need to solve the Schrödinger equation of the multilayer system in the one channel one-dimensional (1D) approximation, commonly used when the transverse translational invariance holds. The valence and conduction band-edge modulation leads to the specific potential profiles shown in Fig. 1, where square barrier potential shapes, produced by the alternating semiconductor layers, are assumed.

To determine the $In_xGa_{1-x}N$ valence and the conduction-band offsets ΔE_v and ΔE_c we use the widely known formula

$$\Delta E_v = \frac{1}{3}[E_{g,\mathrm{InN}}x - E_{g,\mathrm{GaN}}(1-x) - x(1-x)B_w] = \frac{1}{2}\Delta E_c, \tag{8}$$

where $E_{g,\mathrm{InN}}$ and $E_{g,\mathrm{GaN}}$ are the energy gaps of InN and GaN, respectively, and B_w the bowing parameter. Notice that $E_{g,\mathrm{InN}}$ and $E_{g,\mathrm{GaN}}$ may, in general, be replaced by the corresponding energy gaps in the barrier and in the valley of the superlattice of interest.

To solve the Schrödinger problem for the superlattice, plus the two-layered heterostructures on the left- and right-hand sides, we use the transfer matrix method and follow the strategy and formulas of he theory of finite periodic systems.[12] We first obtain the single-cell transfer matrix

$$M = M_{wb}M_b(l_b)M_{bw}M_w(l_w) = \begin{pmatrix} \alpha & \beta \\ \alpha^* & \beta^* \end{pmatrix} \tag{9}$$

where $M_w(l_w)$ and $M_b(l_b)$ are the transfer matrices which propagate the state vectors from one point to another in the same well and in the same barrier. M_{bw} and M_{wb} are the transfer matrice for the well $\rightarrow$ barrier and barrier $\rightarrow$ well interfaces. We then use the formulas

$$\alpha_j^* = p_j - \alpha p_{j-1}, \tag{10}$$

$$\beta_j = \beta^{-1} p_{j-1}, \tag{11}$$

for the transfer matrix M_j relating state vectors at any two points z_0 and $z_j = z_0 + jl_c$ separated by j cells of length l_c. For energies below the band edge of the cladding layers (V_e^c and V_h^c) the boundary conditions require exponentially decaying wave functions at the ends of the superlattice. This imposes further restrictions on the transfer matrices.

Although the transfer matrix of the whole system could be built as

$$M = M_R M_{Rs} M_s M_{sL} M_L \tag{12}$$

and can then be explicitly obtained, we have found that in order to calculate the miniband structure and the wave functions with a precision as high as 10^{-7} eV, it is sufficient to consider the transfer matrix

$$M = M_{Rs} M_s M_{sL} \tag{13}$$

where M_{sL} and M_{Rs} refer to the left and right cladding layers.

For a system bounded with finite walls,[13] the eigenfunctions at any point z in the $(j+1)$-th cell, are given by

$$\Psi_{\mu,\nu}(z) = \vec{\varphi}_{\mu,\nu}(z) + \overleftarrow{\varphi}_{\mu,\nu}(z) = \vec{\varphi}[\mathrm{mod}(z, l_c)]\left[\mathrm{Re}(\alpha_j + \beta_j) + \frac{\kappa_c}{k}\mathrm{Im}(\beta_j - \alpha_j)\right], \tag{14}$$

where the functions $\vec{\varphi}_{\mu,\nu}(z)$ and $\overleftarrow{\varphi}_{\mu,\nu}(z)$ represent the right and left propagating functions. Assuming $E < V_i^c$ (i=e,h), the eigenvalues are obtained from

$$\frac{\kappa_c^2 - k_0^2}{2\kappa_c k_0}\mathrm{Im}\ \alpha_n - \frac{\kappa_c^2 + k_0^2}{2\kappa_c k_0}\mathrm{Im}\ \beta_n + \mathrm{Re}\ \alpha_n = 0, \tag{15}$$

where α_n and β_n are the n-cells superlattice transfer matrix elements [Eqs. (10) and (11)], $\kappa_e^2 = 2m_{\|q}^*(V_i^c - E)/\hbar^2$, and $k_0^2 = 2m_{\|q}^* E/\hbar^2$ is the wave vector at $z = z_0$. Having obtained these eigenvalues we can now evaluate the corresponding eigenfunctions. In the one propagating mode limit considered here, the polynomial p_m reduces to the well-known Chebyshev polynomial of the second kind U_m. Using the previous analytic formulas the intra- and inter-band radiative transition probabilities can accurately be calculated.

B. Intra- and inter-band radiative transitions and the PL spectrum

For a system like the one shown in Fig. 1, which is similar to the heterostructures reported in the literature,[1–8] we plot the miniband structure shown in Fig. 3. In these calculations, the effect of the charge polarization has been neglected but will be considered at the end of Sec. III. The ground-state bands for electrons and holes are extremely narrow and become denser as the number of cells in the superlattice increases. In this figure, we also show the lowest-miniband energy levels $E_{1,\nu}$ ($\nu = 1,2,...,n-1$), for $n=6$.

In general, to identify the various radiative processes, it is convenient to consider the exciton field

$$\Psi(z) = \sum_{\mu,\nu} \Psi^c_{\mu,\nu}(z) a_{\mu,\nu} + \sum_{\mu',\nu'} \Psi^v_{\mu',\nu'}(z) b^+_{\mu',\nu'} \equiv \varphi_c(z) + \phi^+_\nu(z) \tag{16}$$

with $a_{\mu,\nu}$ and $b_{\mu,\nu}$ the electron and hole annihilation operators in the ν-th state of the μ-th miniband, respectively. In terms of this field, the particle-field interaction amplitude becomes

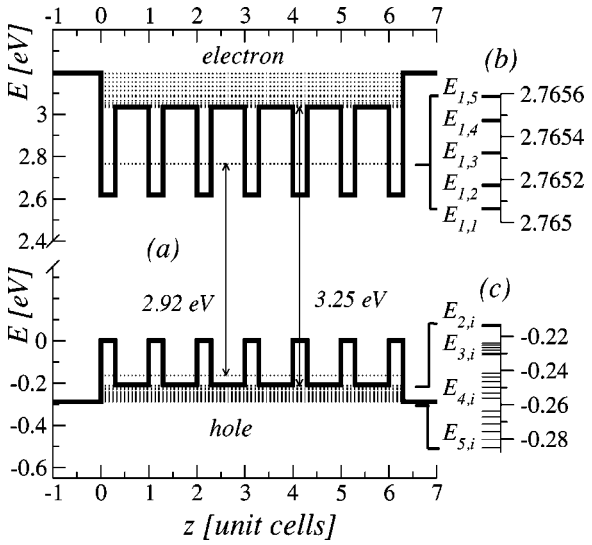

FIG. 3. (a) Miniband structure obtained for the heterostructure reported by Nakamura *et al.* (b) Energy levels of the first minibands in the conduction band. (c) Minibands above the hole barriers.

$$\sum_{q=e,h}\langle H_{Iq}\rangle=\sum_{q=e,h}\frac{i\hbar e}{m^*_{\|q}c}\int dz\Big[\varphi_c^+(z)\mathbf{A}(z)\frac{\partial}{\partial\mathbf{r}}\varphi_c(z)+\varphi_c^+(z)\mathbf{A}(z)\frac{\partial}{\partial\mathbf{r}}\phi_v^+(z)+\phi_v(z)\mathbf{A}(z)\frac{\partial}{\partial\mathbf{r}}\varphi_c(z)+\phi_v(z)\mathbf{A}(z)\frac{\partial}{\partial\mathbf{r}}\phi_v^+(z)\Big]. \tag{17}$$

In the lowest order, the first and fourth terms in this equation correspond to intraband and intraminiband transitions which emit or absorb infrared photons. The remaining terms produce higher-energy transitions. The second term accounts for the absorption process while the third term describes the annihilation of an exciton with the emission of a blue photon. We are interested in the third term contribution. More precisely, our purpose is the calculation of

$$\sum_{q=e,h}\frac{i\hbar e_q}{m^*_{\|q}c}\int dz\,\phi_v(z)\mathbf{A}(z)\frac{\partial}{\partial\mathbf{r}}\varphi_c(z)$$

$$=\sum_{q=e\text{-}h}\frac{i\hbar e_q}{m^*_{\|q}}\sum_{\nu,\nu',\mu,\mu',s,\lambda}g_s d^+_{s,\lambda}a_{\mu,\nu}b_{\mu'\nu'}(\mathbf{e}_{s,\lambda}\cdot\mathbf{K}_s)\times\int dz\Psi^v_{\mu',\nu'}(z)e^{i\mathbf{K}_s\cdot\mathbf{r}}\frac{\partial}{\partial z}\Psi^c_{\mu,\nu}(z), \tag{18}$$

where $g_s=\sqrt{2\pi\hbar c^2/\omega_s\Omega}$. Higher-order transitions, which consist of infrared emissions followed by a recombination process, are neglected.

To compare our results to the PL measurements in Refs. 7 and 8 we calculate the optical susceptibility described by

$$\chi=\sum_{\nu,\nu',\mu,\mu'}\frac{\left|\int dz\Psi^{\nu}_{\mu'\nu'}(z)\frac{\partial}{\partial z}\Psi^c_{\mu,\nu}(z)\right|^2}{(\omega_s-E_{\mu\nu}+E_{\mu'\nu'})^2+\Gamma^2}, \tag{19}$$

where Γ is introduced as a phenomenological level broadening constant.

At variance with the current approaches to calculate the radiative emission we have here a precise procedure to determine the eigenfunctions $\Psi^c_{\mu,\nu}(z)$ and $\Psi^v_{\mu',\nu'}(z)$ (Appendix A). The possibility of knowing these quantities provides us with the ability to theoretically calculate the radiative transitions.

In this approach, we also include the possibility of having additional confinement in the transverse direction. The explicit analysis of the excitonic energy spectrum in a quantum dot was studied in various references. We consider the model and results of Refs. 14–16. A summary is presented in Appendix B. The quantum dot confining contribution and the charge polarization effect are shown here to be crucial as tuning parameters to determine the exact value of the recombination energy measured experimentally.

III. RESULTS AND DISCUSSION

For the system in Fig. 1, frequently used in the literature,[1–8] the well and barrier widths are taken as $l_w=25$ Å and $l_b=60$ Å. If we consider the energy gaps $E_{g,\mathrm{GaN}}=3.485$ eV and $E_{g,\mathrm{InN}}=1.9$ eV at 20 K,[17] and the bowing parameter $B_w=3.4$ eV,[18,19] the barrier heights V_i $(i=e,h)$ in the superlattice become 0.4165 and 0.2083 eV, respectively, while the potentials V_i^c in the cladding layers measured from the band edges are 0.5783 and 0.2891 eV. The effective masses in the active region are determined from a linear interpolation. For the electron we interpolate between $m^*_{\|,e,\mathrm{GaN}}=0.16m_0$ and $m^*_{\|,e,\mathrm{InN}}=0.1m_0$ and for the (heavy or light) hole between $m^*_{\|,h\mathrm{GaN}}=2.0m_0$ and $m^*_{\|,h\mathrm{InN}}=1.67m_0$,[20–23] where m_0 is the electron mass. For these parameters, we plot the miniband structure shown in Fig. 3(a). For energies below the barriers' potentials V_e and V_h, we find isolated and narrow minibands with energy levels in the interval between 2.765 and 2.7656 eV in the conduction band [Fig. 3(b)], and between -0.165142 and -0.165144 eV in the valence band. These minibands contain $n-1$ levels where n is the number of cells in the superlattice. Above the barriers we have many subbands with small energy gaps. The subband widths increase with increasing energy. At the same time, the energy level distance increases, while the subbands approach each other. Each miniband contains $n+1$ energy levels [see Fig. 3(c)].[24] A similar structure can be observed in the conduction band.

The distance between the lowest miniband and the set of subbands above the barriers, especially in the conduction band, is essential to account for the experimental PL results. For the system under study the lowest-conduction subband and the highest-valence subband are separated by approximately 2.92 eV, while the separation between the next subbands in the conduction and valence band is 3.25 eV (Fig. 3). These subband gaps are responsible for the two PL peaks observed by Narukawa *et al.*, which are separated by approximately 0.235 eV. On the other hand, the position in energy of the lowest-energy peak is determined by the superlattice parameters and the exciton's lateral confinement energy, which for quantum dots of different sizes, is of the

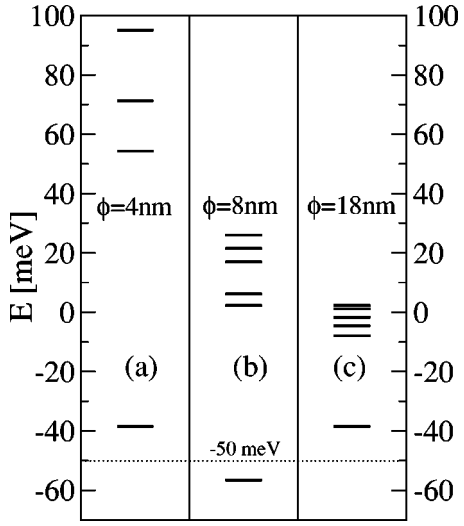

FIG. 4. Exciton lateral confinement energy for symmetric quantum dots of (a) 4 nm, (b) 8 nm, and (c) 18 nm of diameter. The lowest level has an energy of the order of -50 meV.

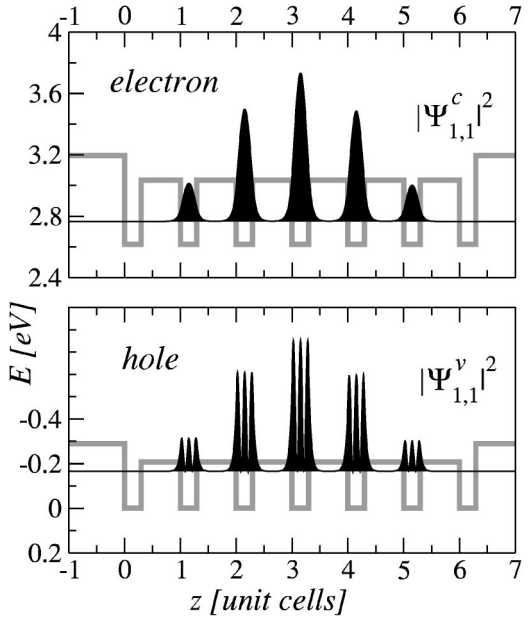

FIG. 5. Wave-functions $\Psi^c_{1,1}$ and $\Psi^v_{1,1}$ for the first energy level of the first subband in the conduction and valence band. For these wave functions the electron and hole are localized in the interior of the quantum wells.

order of -50 meV, as shown in Fig. 4. In this calculation, we have used $m_{\perp,e,\mathrm{GaN}}=0.23m_0, m_{\perp,e,\mathrm{InN}}=1.67m_0, m_{\perp,h,\mathrm{GaN}}=2.04m_0$, and $m_{\perp,h,\mathrm{InN}}=1.61m_0$,[20,21] $\epsilon=9.0$.[11]

To obtain the optical susceptibility, we calculate all the possible first-order transitions between the conduction and the valence subbands. We evaluate the integrals in the numerator of Eq. (19), using the exact forms of the eigenfunctions given in Appendix A. In this way we obtain the two main peaks with a separation of 0.324 eV (Fig. 2). To account for the correct intensities we would have to calculate the higher-order transitions in order to determine the occupation probability of each state. Although this might be interesting, the first-order calculation is sufficient to gather information on the relative distance of the main peaks observed experimentally.

The specific values of the transition probabilities depend on the subband and intraband indexes in the wave functions $\Psi^c_{\mu,\nu}(z)$ and $\Psi^v_{\mu',\nu'}(z)$. By plotting the square of the absolute values of these eigenfunctions we can infer the main properties of the selection rules and transition probabilities. In Fig. 5 we show the wave functions $\Psi^c_{1,1}(z)$ and $\Psi^v_{1,1}(z)$ that correspond to the first energy levels $E^c_{1,1}$ and $E^v_{1,1}$ in the first miniband of the conduction and valence bands, respectively. The electron and hole that occupy these states, with energies below the barrier potential, are localized in the quantum well regions. On the other hand, in Fig. 6 we notice that the electron in the state $\Psi^c_{2,2}(z)$, with energy $E^c_{2,2}$ between the barrier potential V_e and the cladding layer potential V^c_e, is localized mainly in the barriers' region. This same phenomenon occurs in the valence band. The transition probability values depend strongly on the overlapping of the wave functions and their derivatives. Thus, the recombination processes that take place between matching states are more likely to happen than those between states that do not match, i.e., a transition of the form $\Psi^c_{\nu,\mu}(z)\rightarrow\Psi^v_{\nu',\mu'}(z)$ will have higher probabilities for $\nu=\nu'$. This selection rule gives rise to the two PL peaks observed in Fig. 2, where the calculated optical susceptibility (solid line -), normalized to fit the experimental data (dotted line ...), is shown together with a curve that takes into account the shift induced by the charge polarization effect (dashed line ·-·-) as explained below

The miniband structure that results when the sectionally constant potential is replaced by a parabolic band-edge modulation, as suggested in Ref. 11, can also be calculated using the TFPS (Figs. 7 and 8). The main consequences of changing the band-edge shape are (1) a repulsion of the low-

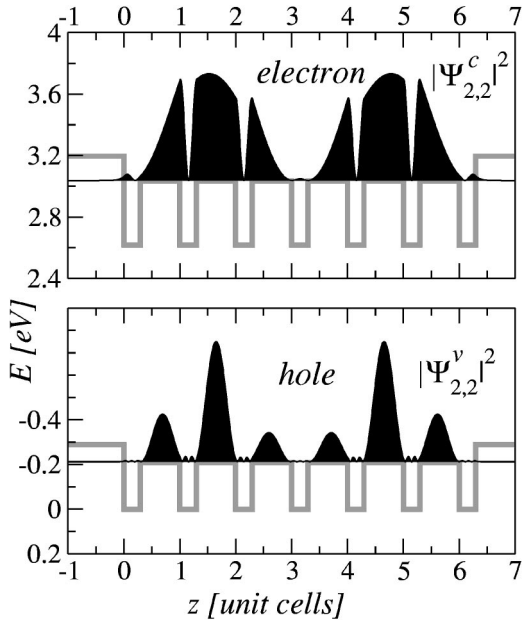

FIG. 6. Wave-functions $\Psi^c_{2,2}$ and $\Psi^v_{2,2}$ for the second energy level of the second subband in the conduction and valence band. For these wave functions the electron and hole are mainly in the interior of the barriers.

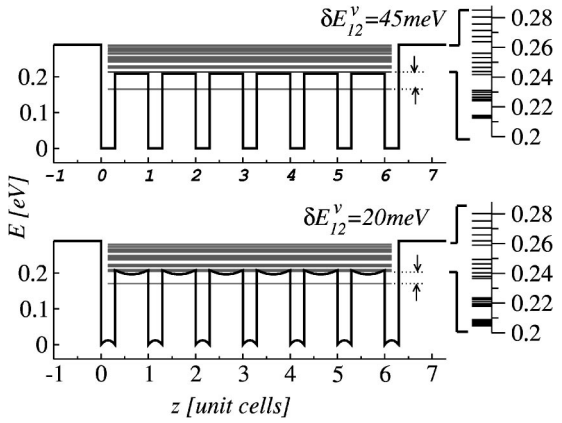

FIG. 7. Miniband structure for the flat band profile (up) and the parabolic band-edge modulation (down) in the valence band.

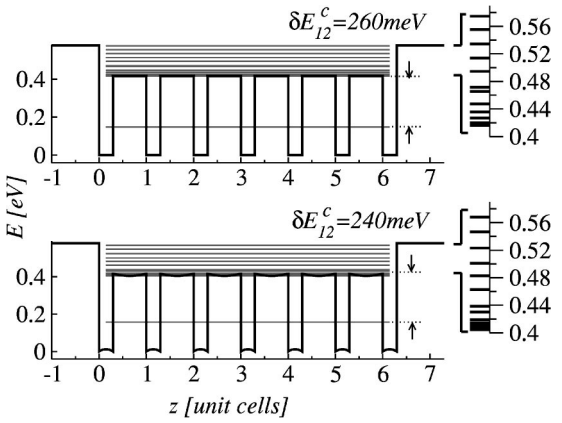

FIG. 8. Miniband structure for the flat band profile (up) and the parabolic band-edge modulation (down) in the conduction band.

energy conduction and valence subbands, produced by the increased potential in the bottom of the quantum well and (2) because of the concavity in the upper part of the barriers' potential, an attraction of the subbands above the barrier.

Since, as mentioned before, the main contribution to the optical response comes from the transition $E^c_{1,\nu}\rightarrow E^v_{1,\nu}$ for the first peak and from $E^c_{2,\nu}\rightarrow E^v_{2,\nu}$ for the second peak, it is clear that the distance ΔE_{21} between the two peaks is approximately the separation between the first and the second conduction subbands δE^c_{21} plus the corresponding separation in the valence subbands δE^v_{21}, i.e.

$$\Delta E_{21}\approx(E^c_{2,\nu}-E^c_{1,\nu})+(E^v_{2,\nu}-E^v_{1,\nu})=\delta E^c_{21}+\delta E^v_{21}. \quad (20)$$

It is possible to infer from Figs. 7 and 8 that this quantity changes from $\Delta E_{2,1}=0.305$ eV, for sectionally constant band-edge potential profile to $\Delta E_{2,1}=0.26$ eV when the band edge has a parabolic modulation. We expect that this relative reduction of about 45 meV in the transition energies, will account for the difference between our theoretical predictions for sectionally constant band edge and the experimental results, in a more precise and complete calculation. A first-order calculation of this reduction is shown in Fig. 2 (dashed line ·-·-).

IV. CONCLUSIONS

We studied an exciton confined in the lateral and longitudinal directions of the AlGaN/GaN/$(In_{x_1}Ga_{1-x_1}N/In_{x_2}Ga_{1-x_2}N)^n$/GaN/AlGaN superlattice in the active region of a blue laser device. For negligible z dependence of the Coulomb interaction these degrees of freedom where decoupled. We solved the Schrödinger equation for the superlattice and determined the exact energy eigenvalues and eigenfunctions. Using these quantities the interband transition amplitudes and the optical susceptibility were calculated. The discrepancy between our calculations and the PL experimental measurements by Narukawa *et al.* appear to be related to the charge polarization effect. Although here we present results for a specific set of device parameters, the expressions and the theory, might be applied to design and to get an important insight of the physics for a great variety of other configurations.

ACKNOWLEDGMENTS

The authors are grateful to Jaime Grabinsky, Herbert Simanjuntak, Eugenio Ley-Koo, William Marshall, and Maríalaura Sasso for the critical reading of the manuscript. This work was supported by CONACyT México Project No. E-29026.

APPENDIX A: WAVE FUNCTION

The electron's wave vectors in the various regions of the heterostructure are given by

$$k_i=\frac{1}{\hbar}\sqrt{\frac{E-V_i}{2m_i}}, \quad i=c,w,b, \quad (A1)$$

where the indexes c, w and b stand for cladding layer, well, and barrier. The wave function is given by

$$\Psi^{c,v}_{\mu,\nu}(z)=\begin{cases}\eta^T\Phi(z), & -\infty<z\leqslant 0,\\ \eta^T M_w(z-jl_c)M_j M_{sL}\Phi(0) & jl_c<z\leqslant jl_c+l_w,\\ \eta^T M_b(z-l_w-jl_c)M_{bw}M_w(l_w)M_j M_{sL}\Phi(0), & jl_c+l_w\leqslant z<(j+1)l_c,\\ \eta^T M_w(z-nl_c)M_n M_{sL}\Phi(0), & nl_c\leqslant z<nl_c+l_w,\\ \eta^T M_c(z)M_{Rs}M_w(l_w)M_n M_{sL}\Phi(0) & nl_c+l_w\leqslant z<\infty.\end{cases} \quad (A2)$$

where

$$M_{sL}=\frac{1}{2ik_w}\begin{pmatrix} k_c+ik_w & -k_c+ik_w \\ -k_c+ik_w & k_c+ik_w \end{pmatrix},$$

$$M_{Rs}=\frac{1}{2k_c}\begin{pmatrix} k_c+ik_w & k_c-ik_w \\ k_c-ik_w & k_c+ik_w \end{pmatrix},$$

$$M_c(z)=\begin{pmatrix} e^{k_c z} & 0 \\ 0 & e^{-k_c z} \end{pmatrix},$$

$$M_w(z)=\begin{pmatrix} e^{ik_w z} & 0 \\ 0 & e^{-ik_w z} \end{pmatrix},$$

$$M_{bw}=\frac{1}{2k_b}\begin{pmatrix} k_b+ik_w & k_b-ik_w \\ k_b-ik_w & k_b+ik_w \end{pmatrix}, \tag{A3}$$

$$M_b(z)=\begin{pmatrix} e^{ik_b z} & o \\ 0 & e^{-ik_b z} \end{pmatrix},$$

$$M_{wb}=\frac{1}{2ik_w}\begin{pmatrix} k_b+ik_w & -k_b+ik_w \\ -k_b+ik_w & k_b+ik_w \end{pmatrix},$$

$$\Phi(z)=\begin{pmatrix} e^{k_c z} \\ 0 \end{pmatrix}, \quad \eta=\begin{pmatrix} 1 \\ 1 \end{pmatrix},$$

and $M_j=M_{wb}M_b(l_b)M_{bw}M_\alpha(l_w)$.

APPENDIX B: QUANTUM DOT CONTRIBUTION

The transverse part of the Schrödinger equation can be written in the center of mass (COM) and relative coordinates. The corresponding Hamiltonians in terms of ladder operators are

$$H_{\mathrm{COM}}=\hbar\omega_x(A_x^\dagger A_x+1/2)+\hbar\omega_y(A_y^\dagger A_y+1/2), \tag{B1}$$

and

$$H_{\mathrm{rel}}=\hbar\omega_x(a_x^\dagger a_x+1/2)+\hbar\omega_y(a_y^\dagger a_y+1/2)-\frac{e^2}{\epsilon r}, \tag{B2}$$

where $A_i^\dagger$, A_i, $a_i^\dagger$, and a_i $(i=x,y)$ are the harmonic oscillator's raising and lowering operators constructed from the center of mass and relative coordinates, respectively.

To solve the Schrödinger equation for H_{rel} we use the harmonic oscillator's basis. The excitonic energy spectrum is obtained by numerical diagonalization (Fig. 4).

[1] Shuji Nakamura, Takashi Mukai, Masayuki Senoh, Shin-ichi Nagahama, and Naruhito Iwasa, J. Appl. Phys. **74**, 3911 (1993).
[2] Shuji Nakamura, Takashi Mukai, and Masayuki Senoh, J. Appl. Phys. **76**, 8189 (1994).
[3] Shuji Nakamura, Masayuki Senoh, Naruhito Iwasa, Shin-ichi Nagahama, Takao Yamada, and Takashi Mukai, Jpn. J. Appl. Phys., Part 2 **34**, L1332 (1995).
[4] Shuji Nakamura, Masayuki Senoh, Shin-ichi Nagahama, Naruhito Iwasa, Takao Yamada, Toshio Matsushita, Hiroyuki Kiyoku, and Yasunobu Sugimoto, Jpn. J. Appl. Phys., Part 2 **35**, L74 (1996).
[5] Shuji Nakamura, Masayuki Senoh, Shin-ichi Nagahama, Naruhito Iwasa, Takao Yamada, Toshio Matushita, Hiroyuki Kiyoku, and Yasunobu Sugimoto, Jpn. J. Appl. Phys., Part 2 **35**, L217 (1996).
[6] F. A. Ponce and D. P. Bour, Nature (London) **386**, 351 (1997).
[7] Yukio Nawakami, Shizuo Fujita, Shigeo Fujita, and Shuji Nakamura, Phys. Rev. B **55**, R1938 (1997).
[8] Yukio Narukawa, Yoichi Kawakami, and Shigeo Fujita, and Shuji Nakamura, Phys. Rev. B **59**, 10 283 (1999).
[9] P. Pereyra and S. Ulloa, Phys. Rev. B **61**, 2128 (2000).
[10] .F. Assaoui and P. Pereyra, J. Appl. Phys. **91**, 5163 (2002).
[11] D. Goepfert, E. F. Schuber, A. Osinsky, P. E. Norris, and N. N. Faleev, J. Appl. Phys. **88**, 2030 (2000).
[12] P. Pereyra, Phys. Rev. Lett. **80**, 2677 (1998).
[13] P. Pereyra, IC/2000/124, www.ictp.trieste.it. ~pub_off.
[14] V. Halonen, T. Chakraborty, and P. Pietiläinen, Phys. Rev. B **45**, 5980 (1992).
[15] J. Song and S. E. Ulloa, Phys. Rev. B **52**, 9015 (1995).
[16] A. Wojs and P. Hawrylak, Phys. Rev. B **51**, 10 880 (1995).
[17] W. Shan, T. J. Schmidt, X. H. Yang, S. J. Hwang, J. J. Song, and B. Goldemberg, Appl. Phys. Lett. **66**, 985 (1985).
[18] Shuji Nakamura, J. Vac. Sci. Technol. A **13**, 6844 (1995).
[19] H. Amano, Mater. Res. Soc. Sump. Proc. **449**, 1143 (1997).
[20] Y. C. Yeo, T. C. Chong, and M. F. Li, J. Appl. Phys. **83**, 1429 (1998).
[21] K. Kim, W. R. L. Lambrecht, B. Segall, and M. Schilfgaarde, Phys. Rev. B **56**, 7363 (1997).
[22] M. Suzuki, T. Uenoyama, and A. Yanase, Phys. Rev. B **52**, 8132 (1995).
[23] A. Majewski, M. Städele, and P. Vogl, in *III-IV Nitrides. MRS Symposia Proceedings, Materials Research Society, T. Moustakas, 1987*, edited by B. Monemar, I. Akasaki, and F. Ponce, p. 887.
[24] P. Pereyra (unpublished).